

Atomistic Simulation Studies on the Dynamics and Thermodynamics of Nonpolar Molecules within the Zeolite Imidazolate Framework-8

Evangelia Pantatosaki,^{†,‡} Federico G. Pazzona,[‡] Gregory Megariotis,[‡] and George K. Papadopoulos^{*,‡}

IRCELYON, Institut de Recherches sur la Catalyse et l'Environnement de Lyon, CNRS, Université de Lyon, 2 Avenue A. Einstein, 69626 Villeurbanne, France, School of Chemical Engineering, National Technical University of Athens, 9 Heroon Polytechniou Street, 157 80 Athens, Greece

Received: December 3, 2009; Revised Manuscript Received: December 28, 2009

Statistical-mechanics-based simulation studies at the atomistic level of argon (Ar), methane (CH₄), and hydrogen (H₂) sorbed in the zeolite imidazolate framework-8 (ZIF-8) are reported. ZIF-8 is a product of a special kind of chemical process, recently termed as reticular synthesis, which has generated a class of materials of critical importance as molecular binders. In this work, we explore the mechanisms that govern the sorption thermodynamics and kinetics of nonpolar sorbates possessing different sizes and strength of interactions with the metal–organic framework to understand the outstanding properties of this novel class of sorbents, as revealed by experiments published elsewhere. For this purpose, we have developed an in-house modeling procedure involving calculations of sorption isotherms, partial internal energies, various probability density functions, and molecular dynamics for the simulation of the sorbed phase over a wide range of occupancies and temperatures within a digitally reconstructed unit cell of ZIF-8. The results showed that sorbates perceive a marked energetic inhomogeneity within the atomic framework of the metal–organic material under study, resulting in free energy barriers that give rise to inflections in the sorption isotherms and guide the dynamics of guest molecules.

1. Introduction

Over the past decade, organic synthesis has given a vast rise to oriented design and production of new classes of metal–organic crystalline materials based on framework types that resemble zeolites. This strategy of synthesis engineering¹ toward target structures has created materials such as the metal–organic frameworks (MOFs), which mainly because of their high uptake capacities to hydrogen, methane, and carbon dioxide have become one of the most popular classes of porous materials. Although their thermal stability, a key characteristic for a technologically important sorbent, can be considered moderate compared to zeolites, the reticulated process of their synthesis makes them superior as compared to the conventional aluminosilicate crystals. The resulting organic zeolite analogues are characterized by large pore sizes, high apparent surface areas, and a chemically active interior, which provide them with exceptional properties as sorbents capable of hosting large amounts of sorbate molecules of a broad span of sizes.

The great success of these crystalline solids as molecular binders is due to processes that involve appropriate linking of selected molecular blocks together, by building them on geometrically well-defined morphologies.^{1–4} Moreover, the high availability of these compounds for further chemical modification of their linking units can lead to the creation of a whole series of homologues possessing various pore widths. A recent example is the linking of the organic groups through strong covalent bonds in place of metal ions, which has yielded a new

class of materials possessing large pores, known as covalent organic frameworks (COFs).⁵

Another recent advance in the aforementioned reticulation strategy is the synthesis of a subcategory of MOFs, termed as zeolitic imidazolate frameworks (ZIFs), wherein transition metals replace T-atoms, and imidazolate or imidazolate-type links replace oxygen bridges in the conventional aluminosilicate structures.^{6–8} Systematic chemical modification^{6,8} of their substituents has also created a series of homologous ZIF structures characterized by high chemical and thermal stability, based on framework types of either known zeolite topologies, such as sodalite, RHO, MER or even predicted structures.⁶

Scientists from the field of theory and simulation have given insight into molecular dynamics of the sorbed phase in a variety of MOF and COF structures.^{9–18} In contrast, despite the availability of papers reporting experimentally measured high uptake capacities regarding either hydrogen, or the greenhouse gases methane and carbon dioxide in several zeolitic imidazolate structures,^{6,7,19–22} so far, fewer works have dealt with modeling in ZIFs.^{23,24}

In this article, we present statistical-mechanics-based modeling of the sorption thermodynamics and dynamics of selected nonpolar molecules in the recently synthesized^{6,19,25} ZIF-8, first, to investigate the evolution of the sorption equilibrium over a wide range of occupancies of guest molecules, up to saturation; and second, to elucidate the rate and mechanism of motion of guest molecules in the pores of the metal–organic framework under study. Moreover, we examine the applicability of the DREIDING²⁶ and UFF²⁷ force fields for the description of atomic-level interactions between sorbate molecules and framework atoms along with our in-house-built modeling process, previously employed to studies of conventional zeolite frameworks.^{28–30}

* To whom correspondence should be addressed. Phone: +302107723112. Fax: +302107723112. E-mail: gkpap@chemeng.ntua.gr.

[†] Université de Lyon.

[‡] National Technical University of Athens.

TABLE 1: DREIDING²⁶ and UFF²⁷ Interaction Parameters for the Framework Atoms of the ZIF-8

interaction type ^a	DREIDING		UFF	
	ϵ (kcal/mol)	σ (nm)	ϵ (kcal/mol)	σ (nm)
Zn–Zn	0.0550	0.4045	0.1240	0.2462
N–N	0.1450	0.3292	0.0690	0.3261
C–C	0.0950	0.3457	0.1050	0.3431
CH–CH	0.1356	0.3768		
CH ₃ –CH ₃	0.2500	0.3699		
H–H			0.0440	0.2553

^a –CH and –CH₃ groups are treated as united atoms.

Our computer simulation methodology relies upon classical physics with interparticle interactions being calculated through potential functions such as the Lennard-Jones potential. For hydrogen, we employed the quantum mechanical potential function of Feynman–Hibbs³¹ for all interactions of the guest–host system. At this point, we should notice that a good force field must be capable of capturing the essential physico-chemical properties of a system, but it rarely yields accurate results with respect to real experiments; this is especially true for metal–organic materials due to the complexity of their atomic framework. Full-scale ab initio quantum mechanical calculations on a certain material can serve as a reasonable basis toward more sophisticated potential functions. Development of such a force field is well beyond the scope of this article, since we study small nonpolar molecules, and polarizability effects can be neglected. In this study, we employed the two generic force fields mentioned above, which have been used successfully in the MOFs and isoreticular MOF (IRMOF) modeling.¹² No adjustment of potential parameters with respect to sorption experiments to match the measured points has been made in this work.

The zeolitic imidazolate framework was represented as a rigid lattice; the experience gained from the majority of atomistic simulations in which a rigid zeolite model was used is that framework flexibility affects mainly the thermodynamics of long molecules at high loadings (tight fitting) and, hence, their diffusivity. Nonetheless, simulations performed lately by incorporating framework flexibility in the modeling of MOFs have led to the conclusion that lattice flexibility does exert influence on diffusivity,³² although the observed trends regarding the effect of flexibility on the results have been contradictory.^{33,34} In addition, predictions of negative thermal expansion coefficients in IRMOFs as a consequence of the approaching of their organic links with increasing temperature³⁵ do underline the susceptibility of this class of solids to conformation altering.

2. Modeling and Computing Details

2.1. Energetics. The host and guest force field parameters employed in this study are listed in Tables 1 and 2, respectively. Argon and methane molecules were represented as neutral soft spheres, and their interactions were computed by means of the Lennard-Jones potential function,

$$U_{\text{LJ}}(r_{ij}) = 4\epsilon_{ij} \left[\left(\frac{\sigma_{ij}}{r_{ij}} \right)^{12} - \left(\frac{\sigma_{ij}}{r_{ij}} \right)^6 \right] \quad (1)$$

where ϵ_{ij} and σ_{ij} are the strength and size parameters of the interacting i and j atoms, respectively, and r_{ij} is the distance between them.

TABLE 2: Sorbate Interaction Parameters

interaction type	ϵ (kcal/mol)	σ (nm)	parameters notation ^a
Ar–Ar ³⁷	0.2464	0.3380	A1D, A1U
Ar–Ar ³⁸	0.2370	0.3400	A2D, A2U
CH ₄ –CH ₄ ³⁹	0.2939	0.3730	M1D, M1U
CH ₄ –CH ₄ ²⁶	0.3016	0.3775	M2D, M2U
CH ₄ –CH ₄ ⁴⁰	0.3148	0.3720	M3D, M3U
H ₂ –H ₂ ³⁶	0.0725	0.2820	HD, HU

^a Combinations of the guest and host parameters employed: numbers indicate guest model; A, M, and H stand for Ar, CH₄, and H₂, respectively; D and U stand for DREIDING²⁶ and UFF²⁷ host models.

For the H₂ molecule, the classical description of eq 1 is not adequate; for this, the quadratic form of the temperature-dependent effective potential of Feynman and Hibbs is employed:^{28,31}

$$U_{\text{FH}}(r_{ij}) = U_{\text{LJ}}(r_{ij}) + \frac{\hbar^2}{24k_{\text{B}}Tm_{\text{r}}} \left[\frac{\partial^2 U_{\text{LJ}}(r_{ij})}{\partial r_{ij}^2} + \frac{2}{r_{ij}} \frac{\partial U_{\text{LJ}}(r_{ij})}{\partial r_{ij}} \right] \quad (2)$$

The above correction term to U_{LJ} was introduced in view of the formulation of the evolution of a quantum mechanical system as a path integral between two states. The path integral encompasses all the possible paths by which the system can travel between two different configurations in the time interval $\hbar/k_{\text{B}}T$ at the temperature T , where k_{B} is the Boltzmann constant, and $\hbar = h/2\pi$ is the reduced Planck constant, h . Then, by considering a pairwise type potential, such as the one described by eq 1, the mean path can be replaced by the distance, \mathbf{r}_{ij} , between the centers of mass of molecules i and j ; the correction elicits that paths located at \mathbf{r}_j are enveloped inside a Gaussian width.^{31,36} For low temperatures and atomic masses, the distribution around \mathbf{r} becomes widespread; hence, a classical description is not adequate anymore.^{31,36} Equation 2 was used for the H₂–H₂ as well as H₂–ZIF-8 framework atom interactions.

As seen in Table 1, DREIDING provides implicit parameters for each individual hydrogen atom, depending on its chemical environment in the framework. An alternative treatment of hydrogens in the methyl group was also followed to account for the two equiprobable conformations of alkyl, entailing six hydrogen positions as identified by X-ray diffraction.⁶ In this case, hydrogen atoms were parametrized explicitly via UFF. Therefore, potential functions pertaining to these hydrogens were multiplied by a factor of 0.5 on any occasion that UFF was employed. The parameters for the cross interactions were calculated via the Lorentz–Berthelot combining rules.

2.2. Simulation Methodology. The sorption equilibrium experiments of argon, methane, and hydrogen in the ZIF-8 were carried out in the grand canonical Monte Carlo (GCMC) ensemble by means of a typical Metropolis algorithm for the importance sampling of the configuration space. The relative frequencies of displacement, insertion, and deletion moves were 1:1:1, respectively. The sorption isotherm was obtained by computing averages of the number of sorbate molecules, N , over a large number of equilibrated configurations, as a function of the fugacity, f (converted to pressure in the graphs). The relation of the fugacity of the bulk phase with the externally imposed in GCMC chemical potential of the sorbed phase μ_{s} at the temperature T is derived through the equality of the chemical potentials of the two phases, leading to

$$\mu_s = \mu_b = k_B T \ln \left[\frac{f \Lambda^3}{k_B T} \right] \quad (3)$$

where Λ is the de Broglie thermal wavelength.

The potential energy due to cross interactions was pretabulated through eqs 1 and 2 on a three-dimensional grid of 0.02 nm spacing over the entire unit cell. This technique reduced the CPU time significantly and thus allowed efficient phase space sampling by including a larger number of unit cells in the simulation box.^{28–30} The cutoff used for the computation of the potential energy was 1.55 nm for both stochastic and dynamics simulations. The sorption computer experiments needed 10^8 iterations in a simulation box consisting of eight unit cells ($2 \times 2 \times 2$ in the x , y , and z direction) for all runs.

Equilibrium molecular dynamics (MD) simulations were carried out in the canonical (NVT) ensemble for argon and hydrogen in the ZIF-8 to produce molecular trajectories for the computation of the mean squared molecular displacements. Configurations obtained from GCMC runs at the desired density were used as initial configurations for dynamics, using eight unit cells per simulation box, as in the case of Monte Carlo. For the numerical integration of the equation of motion, MD runs were conducted up to a time length of 10 ns by means of the leapfrog algorithm under the Nosé–Hoover thermostat scheme⁴¹ using a time constant of 0.1 ps; the integration step was 1 fs to ensure elimination of the energy drift.

From the time evolution of the position vectors of the center of molecular mass, \mathbf{r} , the mean square displacement,

$$\langle r(t)^2 \rangle = \frac{1}{N} \left\langle \sum_{i=1}^N [\mathbf{r}_i(0) - \mathbf{r}_i(t)]^2 \right\rangle \quad (4)$$

averaged over the total of guests, N , was calculated. This quantity plotted with respect to observation time (MSD plot) was utilized to examine the molecular motion of the sorbed phase. From the linear part of the latter plot at large time, t , the self-diffusivity, D_s , can be extracted according to the Einstein equation:

$$D_s = \frac{1}{6N} \lim_{t \rightarrow \infty} \frac{d\langle r(t)^2 \rangle}{dt} \quad (5)$$

3. Results and Discussion

In this section, we present results from Monte Carlo and molecular dynamics computer experiments in the grand canonical (μVT) and canonical (NVT) ensembles, respectively, to gain insight into thermodynamics and kinetics of the sorbed phase of argon, methane, and hydrogen inside the matrix of a digitally synthesized ZIF-8 unit cell. This part aims principally at understanding the capability of the particular metal–organic frameworks to adsorb nonpolar guest molecules, resulting in isotherm curves that may exhibit steep inflections and high saturation uptakes. The presence of such phenomena is supported by a plethora of experimentally measured isotherms at various temperatures, found elsewhere. We also examined various force field parameters for the modeling of the energy map of this sorbent material in combination with selected parameters of the aforementioned gases found in the literature (Tables 1 and 2). Finally, we proceed to probe the sorbate dynamics inside the ZIF-8. To the best of our knowledge, thus

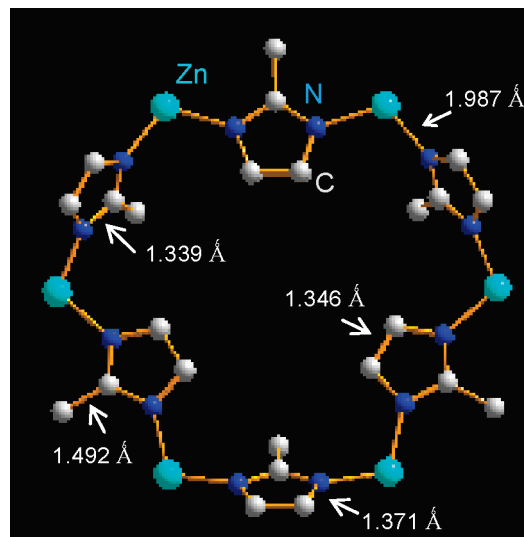


Figure 1. Detail of the atomic framework of the ZIF-8 crystal showing the 2-methylimidazolate organic group link, the Zn, and the N atoms; H atoms are omitted in the figure.

far, no microscopic or macroscopic transport experimental measurements have been performed for these systems.

3.1. Digital Synthesis of the ZIF-8. ZIF-8 has the composition described by the formula $\text{Zn}(\text{mIM})_2$, where mIM denotes the 2-methylimidazolate organic group link. The ZIF-8 unit cell belongs to the sodalite topology; we started its digital representation by means of (i) X-ray diffraction analysis data^{6,19} to locate the atomic positions in the unit cell lattice, and (ii) the $I\bar{4}3m$ space group for the final reproduction of the atomic coordinates, according to their symmetry operations of this space group and their occupancy probabilities in the framework. The thus obtained structure has each zinc ion tetrahedrally coordinated by four nitrogen atoms (ZnN_4) belonging to the imidazolate rings (IM), as illustrated in Figure 1. The shared area formed by the hexagonal windows (effective width: 0.34 nm) and the neighboring cages constitutes the channels that run along the four body-diagonal directions of the ZIF-8 cubic lattice.

The cubic unit cell (edge length: 1.6990 nm) has the formula $\text{C}_{96}\text{H}_{120}\text{N}_{48}\text{Zn}_{12}$. The digitized crystal contains no water molecules. The result of the reconstruction procedure is depicted in Figure 2 where also the primary simulation box employed in all simulations of this work is presented.

XRD measurements⁶ have identified six positions for the hydrogen atoms as a consequence of the two equiprobable orientations of the methyl group; thus, each position has an occupancy probability of 0.5. All the other framework atoms have occupancy probability equal to 1. These probabilities have been properly taken into account in the potential formulas employed for the calculations of the host–guest interactions.

3.2. Computer Experiments. Simulation results for argon in the ZIF-8 at 87 K, using the Lennard-Jones parameters of the two first rows of Table 2 in combination with the DREIDING²⁶ and UFF²⁷ force fields for the atoms on the lattice of the metal–organic material are shown in Figure 3. It is seen that the simulated isotherms via both A1U and A2U sets of parameters overpredict the experimental points over the whole range of pressures. Through the A1D and A2D sets, GCMC predicts earlier the first step of the experimental isotherm, whereas the agreement with the measured values over the low and high pressure region is satisfactory. Moreover, via the A1D set only, simulation captures the second step at its experimental pressure.

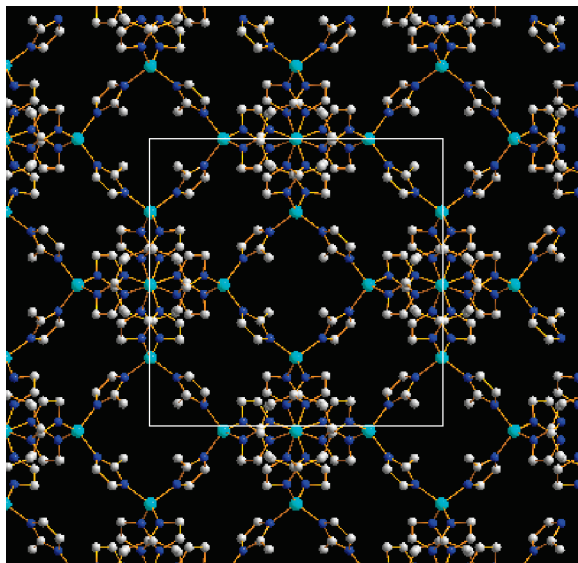


Figure 2. Projection of the primary simulation box of the reconstructed ZIF-8 (containing eight unit cells); the white frame indicates the boundaries of the unit cell; H atoms are omitted from the figure to avoid congestion.

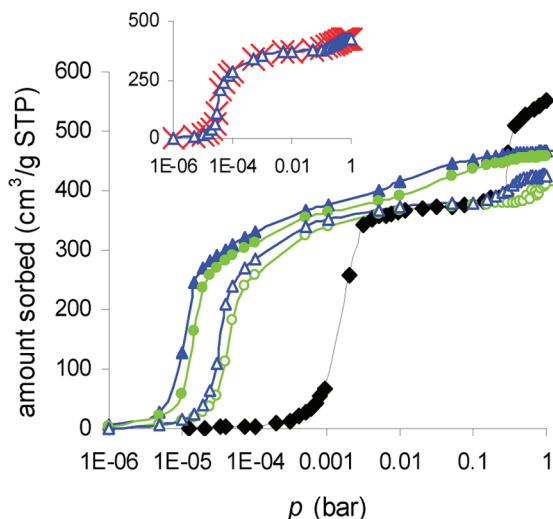


Figure 3. Sorption isotherms of Ar in the ZIF-8 at 87 K obtained by experiment⁶ (black symbols) and GCMC simulations using various model parameters (see Table 2): A1D (open blue triangles), A1U (filled blue triangles), A2D (open green circles), and A2U (filled green circles). Inset shows simulated sorption (open blue triangles)—desorption (red crosses) branches using the A1D set.

An immediate conclusion of the graphs of Figure 3 is that DREIDING is more suitable for the modeling of this metal–organic structure, although failing to predict the first step at its experimental pressure. As already discussed above, the effect of the mobile methyl-imidazolate links can affect the sorption thermodynamics when inflections are present.⁴² The conclusion drawn from the discrepancy between the measured occupancies and our simulation results at saturation may be attributed to the susceptibility of the real framework toward more favorable conformations when higher sorbate amounts are to be hosted in the unit cell. As a consequence, the measured saturation uptake is higher than the predicted value of our simulations in the rigid matrix. The reversibility of the sorption–desorption curve shown in Figure 3 gives no indication of a hysteresis loop. Because no structural variations are allowed under the issue of a rigid model, that finding verifies the absence of capillary condensation phenomena.

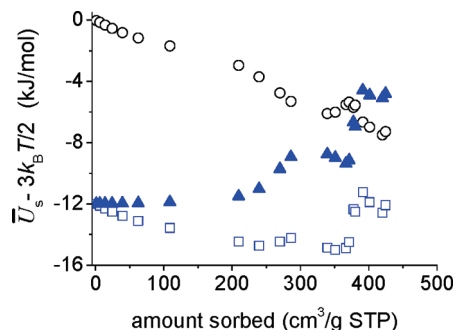


Figure 4. Partial molar configurational internal energy of Ar ($s = 3$) calculated at 87 K via the A1D set of parameters versus occupancy (squares); sorbate–sorbent (triangles) and sorbate–sorbate interactions (circles) are also shown.

In the following lines, a computational study on the energetic content of the adsorption sites of the ZIF-8 with respect to the thermodynamic predictions shown in the above graph will be presented. A usual measure of the energetic inhomogeneity from experimental point of view is the partial molar heat of sorption (isosteric heat), q_{st} , defined as

$$-q_{st} \equiv \bar{H}_s - H_b \quad (6)$$

In a single-component system, H_b is the molar enthalpy of the bulk phase; \bar{H}_s is the partial molar enthalpy of the sorbed phase (in the presence of host species) given by the relation $\bar{H}_s = \bar{U}_s + P\bar{V}_s$; and macron diacritics denote partial molar quantities for the internal energy and volume of the sorbate molecules, under constant pressure and temperature. Whereas in conventional experiments, the quantity q_{st} is measured, in a GCMC simulation, \bar{H}_s can be directly calculated by means of statistical mechanics from the covariance between the number of molecules, N , and enthalpy, divided by the variance in the number of molecules, as follows:

$$\bar{H}_s = \frac{\langle NU_s \rangle - \langle N \rangle \langle U_s \rangle}{\langle N^2 \rangle - \langle N \rangle^2} + P \frac{\langle NV_s \rangle - \langle N \rangle \langle V_s \rangle}{\langle N^2 \rangle - \langle N \rangle^2} \quad (7)$$

The ratio in the second term of the right part of the above equation expresses the partial molar volume, \bar{V}_s , which in the course of a GCMC simulation vanishes. Therefore, by splitting internal energy into its kinetic and configurational, \mathcal{V} (potential energy), components, eq 7 can be put in the form

$$\bar{U}_s - \frac{sk_B T}{2} = \frac{\langle N\mathcal{V} \rangle - \langle N \rangle \langle \mathcal{V} \rangle}{\langle N^2 \rangle - \langle N \rangle^2} \quad (8)$$

where s is the degrees of freedom of the guest molecules and $sk_B T/2$ is their partial molar kinetic energy.

The left part of eq 8 expresses the partial molar configurational internal energy of the sorbed phase. In Figure 4, this quantity is plotted as a function of the argon occupancy in the ZIF-8. In the same graph, the sorbate–sorbate and sorbate–sorbent contributions to the total energy appear; the latter amount is equivalent to the experimentally measured excess energy, reflecting the actual binding energy of the guest molecules with the framework atoms. Around the value of 100 cm³/g STP (cf. Figures 3 and 4), the sorbate–sorbent part starts to increase, exhibiting a peak at the upper value of the isotherm step.

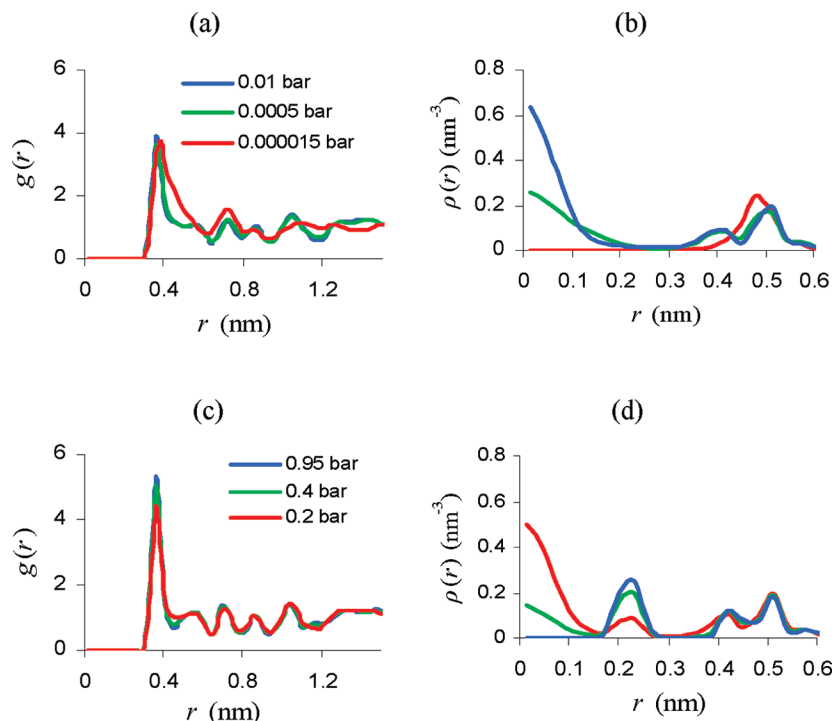


Figure 5. Density distribution functions for various occupancies of Ar in the ZIF-8 at 87 K chosen around the first (top graphs) and second inflection (bottom graphs) of the isotherm shown in Figure 3. (a, c) pair distribution functions $g(r)$; (b, d) density probability distributions $\rho(r)$, calculated with respect to the cage centers.

Subsequently, the energy reaches a plateau and increases steeply again at the point where the second step of the isotherm appears. The observed trend in the calculated partial molar internal energy of argon within the ZIF-8 matrix conforms to the isotherm shape, indicating adsorption sites possessing different energy content.

One- and two-particle probability density distributions $\rho^{(1)}(\mathbf{r}_1)$ and $\rho^{(2)}(\mathbf{r}_1, \mathbf{r}_2)$, respectively, have been utilized in this study to map the location of Ar molecules with varying pressures in this imidazolate framework; more precisely,

$$\rho^{(n)}(\mathbf{r}_1, \dots, \mathbf{r}_n) = \frac{1}{\Xi(\mu, V, T)} \sum_{N=n}^{\infty} \frac{\exp[\mu N/k_B T]}{\Lambda^{3N}(N-n)!} \int d^3r_{n+1} \dots d^3r_N \exp[-\mathcal{V}(\mathbf{r})/k_B T] \quad (9)$$

The above relation expresses the probability for finding a state with one guest molecule located at a certain position, \mathbf{r}_1 ($n = 1$), or the probability of finding a state with one guest molecule located at \mathbf{r}_1 and a second one located at \mathbf{r}_2 ($n = 2$) averaged over all the momentum and configuration space, $\mathbf{r} = \{\mathbf{r}_1, \mathbf{r}_2, \dots, \mathbf{r}_N\}$, of the N molecules inside the ZIF-8 unit cell.

In the graphs of Figure 5, the probability density $\rho^{(2)}(\mathbf{r}_1, \mathbf{r}_2)$ was normalized by $\langle N \rangle^2 V^{-2}$ to give the pair distribution function $g^{(2)}(\mathbf{r}_1, \mathbf{r}_2)$. Considering the magnitude $r = |\mathbf{r}_1 - \mathbf{r}_2|$, the two-particle distribution function takes the form of the radial distribution function, $g(r)$. Similarly, in the special case that the singlet probability density, $\rho^{(1)}(\mathbf{r}_1)$, of finding a molecule at positions radially distributed with respect to a certain point, \mathbf{r}_{ref} within the framework, so that $r = |\mathbf{r}_{\text{ref}} - \mathbf{r}_1|$, the $\rho^{(1)}(\mathbf{r}_1)$ is replaced by $\rho(r)$. Otherwise, the $\rho^{(1)}(\mathbf{r}_1)$ is calculated (e.g., Figures 6–8).

From the comparison of the effect of pressure before, within, and after the first step of the argon isotherm, it is seen that the

fluid becomes slightly more structured with increasing pressure, resulting in a narrower nearest-neighbors peak at about 0.36 nm (Figure 5a). In fact, this distance is close to the nearest-neighbor distance of 0.37 nm measured in solid argon.⁴³ An increase in occupancy up to the second isotherm step causes mainly a rise in the coordination number of the fluid (Figure 5c). The observed behavior of the radial distribution function with increasing pressure indicates a rather structured sorbed phase inside the ZIF-8 pores, eliciting existence of adsorption sites with varying degree of occupancy as a result of energetic inhomogeneity effects.

The probability density, $\rho(r)$, of finding a molecule at positions radially distributed around a certain point inside the zeolite framework may provide information on the location of these sites inside the ZIF-8. The evolution of probability density of argon around the center of cages for pressure values before, inside, and after the formation of the first transition shows a steep increase in the number of molecules in the center of the cage as pressure increases, with a simultaneous appearance of two shorter double peaks at 0.4 and 0.5 nm that are close to the square and hexagonal window necks, respectively (Figure 5b). Namely, as loading (sorbate chemical potential) increases, molecules start migrating to a new energetically less favored site at the cavity center.

The evolution of the probability density at higher pressure exhibits a different trend from the sitting transition at the lower pressure (Figure 5d). That is to say, as argon occupancy increases, the density probability at the cavity center decreases until it finally empties after 0.9 bar; at the same time, enhancement of the probability density at 0.2 nm indicates a new site located within a distance of about 1 argon sigma from the bidisperse distribution shown in Figure 5d, thus indicating layer formation.

The reader is reminded that to obtain probability distributions, particles have been binned over volumes between successive

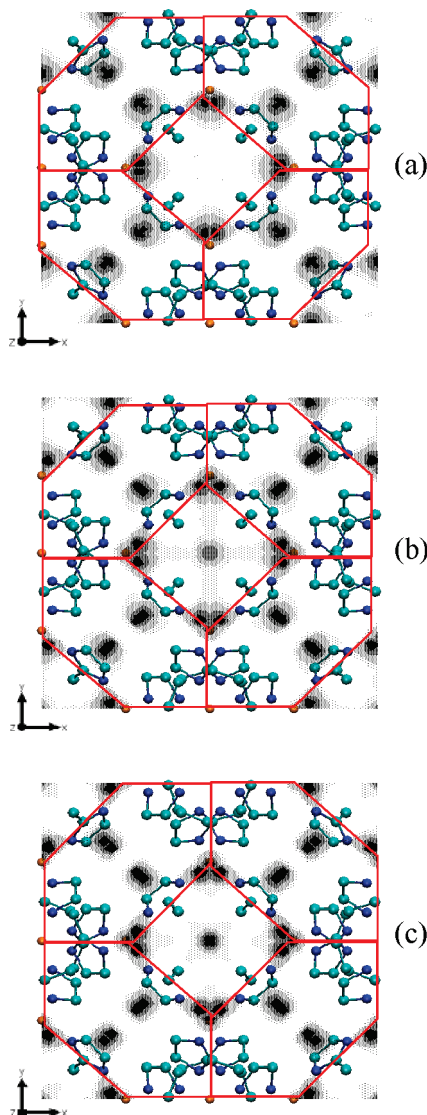


Figure 6. Evolution of isodensity surfaces of Ar at 87 K projected in the x - y plane of the ZIF-8 unit cell under $p = 2.5 \times 10^{-5}$ (a), 5×10^{-4} (b), and 1.0×10^{-2} bar (c), corresponding, respectively, to pressure values before, within, and after the low-pressure transition step (cf. Figures 3 and 5). The isovalues used are 1.0 (light gray), 3.0 (gray), 15.0 (dark gray), and 32.0 nm^{-3} (black). The red frame denotes the positions of the hexagonal and square faces.

spherical cells surrounding a particular reference position. A complementary view to this aspect can be given through the actual singlet probability distribution, $\rho^{(1)}(\mathbf{r}_1)$.

Figures 6–8 present singlet probability density distributions in the form of isodensity surfaces for the three occupancies used in Figures 5 to give a pictorial explanation of the low- and higher-pressure sorption thermodynamics of argon guest molecules. In Figure 6, the population of argon is depicted for various loadings, at positions close to hexagonal and square faces inside the ZIF-8 cavity. The rise in density close to the cage center near saturation is depicted in Figure 7. In Figure 8, isodensity surfaces are presented inside a thin slab containing the center of the cage to illustrate the gradual vacating of argon molecules from the central region as chemical potential increases further, leading eventually to the layered packing shown in Figure 5d.

The mobility of argon at 87 K was estimated through eq 4. In Figure 9, mean square displacements for two occupancies, the one corresponding to a very low pressure value and the other

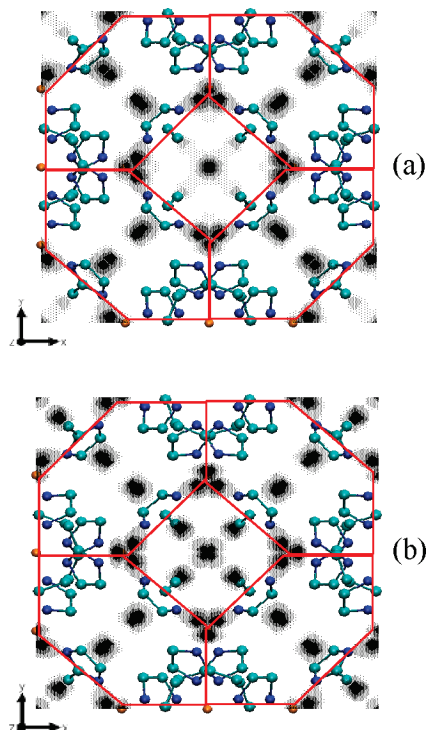


Figure 7. Same as Figure 6 for the high-pressure step. $p = 5 \times 10^{-4}$ (a) and 0.1 bar (b).

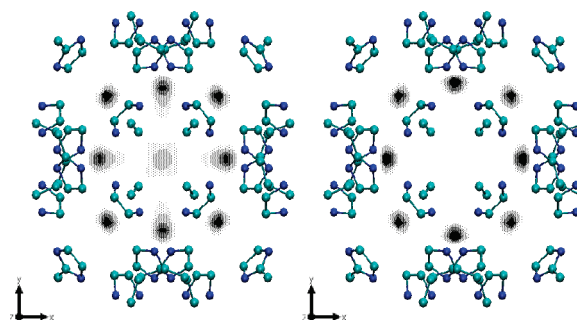


Figure 8. Detail of Figure 7 (probability density seen from a projection plane closer to the cage center) to depict the progressive vacating of Ar molecules before (left) and after (right) the high-pressure transition step.

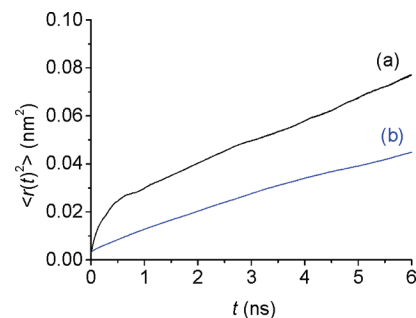


Figure 9. Mean square displacement plots of Ar in the ZIF-8 at 87 K. (a) 10^{-5} bar, $25.6 \text{ cm}^3/\text{g}$ STP ($3.12 \text{ molecules/u.c.}$) and (b) 0.3 bar, $411.4 \text{ cm}^3/\text{g}$ STP ($50.12 \text{ molecules/u.c.}$).

close to saturation, show finally diffusive behavior. The MSD plot at low sorbate concentration exhibits an anomalous part up to 500 ps (Figure 9a). This high molecular displacement at short times may be explained by the different density distributions at the two loadings involved in the above graphs; that is to say, Figure 6a indicates fewer adsorption sites for argon at low occupancies, whereas as chemical potential increases, new

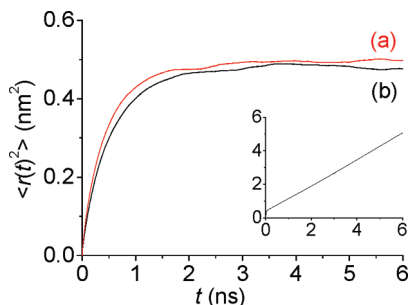


Figure 10. MSD plots of Ar in the ZIF-8 at 87 K: (a) under 5×10^{-5} bar, 259.6 cm³/g STP (31.62 molecules/u.c.) and (b) 2.2×10^{-5} bar, 134.4 cm³/g STP (16.37 molecules/u.c.). The inset depicts the latter set of values at 300 K for the same as before observation time t .

sites inside the cavity become accessible, as seen in the rest graphs of this figure.

Interpreting the above situation on the basis of free energy distribution³⁰ (namely, that a high free energy value corresponds to a low probability of occupying this position and vice versa), one is brought to the conclusion that at infinite dilution, molecules are mostly confined around their initial positions (lowest energy minima), covering long paths at short times before a displacement to an adjacent adsorption site occurs. This happens because free energy barriers between these sites are still high, and therefore, crossing of molecules is infrequent. As a consequence, mean square displacement in the beginning scales faster than linearly with time. As chemical potential increases, the hopping rate becomes much more efficient (see the increased population in Figure 7); therefore, the diffusion propagator takes a Gaussian form earlier, and hence, the MSD plot enters the linear diffusive regime faster (cf. Figures 9a, 9b).

The MSD behavior wherein the low-pressure step takes place also deserves consideration. As observed in Figure 10a and b, the mobility of argon for two concentrations chosen within the transition exceeds the values calculated for any other point of the isotherm far from the step by about 1 order of magnitude. An explanation of this remarkable anomalous MSD behavior at these pressures may be provided by recalling Figures 5 and 6. In particular, as loading increases, the probability density at the sites facing the square windows at a distance of 0.4 nm from the cavity center increases, too, and a simultaneous increase in the probability density between these sites (site-to-site distance, 0.8 nm) is observed (see Figure 6b). Figure 11a shows the particular density isovalue connecting the aforementioned six sites spanning the central part of the cavity interior. The illustrated state clearly denotes a lower free energy barrier between them; therefore, more frequent molecular jumps occur at this area by comparison with neighboring sites, which are separated by high barriers.

This transient restricted motion in the cavity interior results in a mean square displacement that approaches a constant value that corresponds to the characteristic length of about 0.7 nm (see Figure 10a, b). This value is close to the aforementioned site-to-site distance of 0.8 nm, measured along the coordinate axes depicted in Figure 11a.

As the end of the step is approached, the particular isodensity contour starts to dissolve (Figure 6c and 11b). In addition, the free energy of the neighboring sites becomes higher because of the weaker interaction between the argon molecules in the newly created layers and the framework atoms. Consequently, these molecules can pass over the free energy barriers toward adjacent positions much more easily than before, facilitating faster randomization of molecular paths and, hence, linear MSD plots.

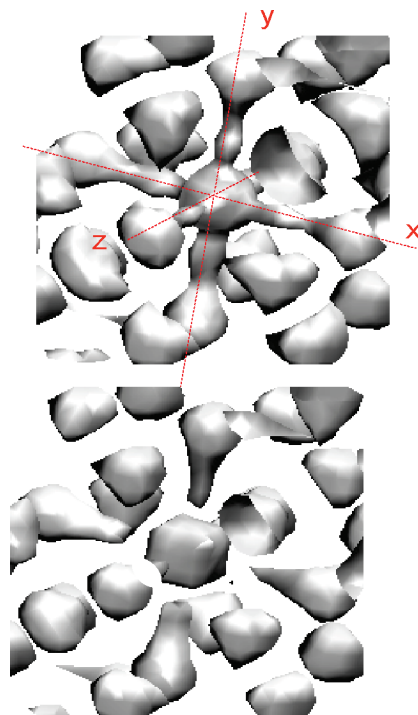


Figure 11. Detail of Figure 6b, isolated for the sake of clarity, illustrating the density isovalue of 1.0 nm⁻³ corresponding to the central region of the cavity interior (top); evolution of the previous state under $p = 5 \times 10^{-3}$ bar (bottom).

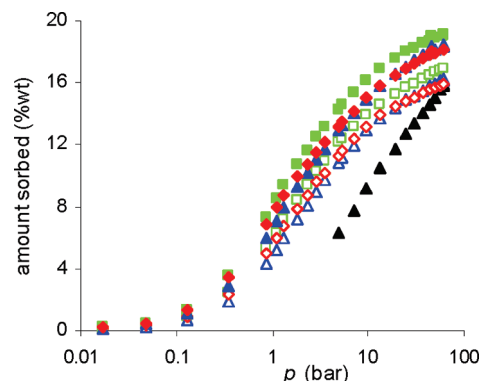


Figure 12. Simulated (colored symbols) and experimental²⁰ (black symbols) sorption isotherms of CH₄ in the ZIF-8 at 240 K; the parameter sets (see Table 2) used in simulations are M1D (open blue triangles), M2D (open red diamonds), M3D (open green squares), M1U (filled blue triangles), M2U (filled red diamonds), and M3U (filled green squares).

Following the same reasoning, the conversion of the anomalous MSD plot shown in Figure 10b to a fully diffusive at 300 K (see inset of Figure 10) can be explained as a result of increasing temperature.

Figure 12 presents grand canonical Monte Carlo results of methane in the imidazolate framework at 240 K for various combinations of guest/host parameters reported in Table 2. The reader is reminded that parameter adjustment with respect to experiments has been avoided in all cases of this study. Among the six sets of potential parameters tested, the set coded as M1D, being a combination of DREIDING force field with the parameters of ref 39 which have been extracted from phase equilibria of liquid methane, proved to be the most satisfactory modeling attempt with respect to the sorption measurements²⁰ illustrated at the same graph. In Figure 13, simulations at various temperatures are compared with experiments found elsewhere.²⁰

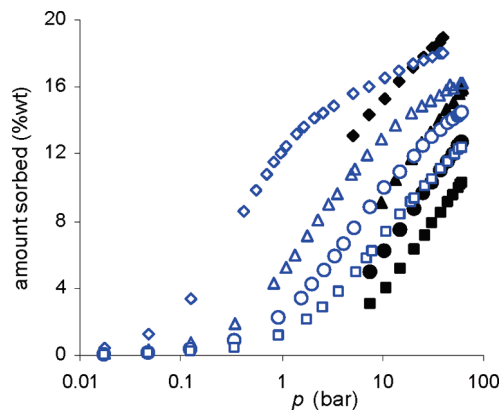


Figure 13. Sorption isotherms of CH_4 in the ZIF-8 from GCMC simulation using the M1D set of parameters (open symbols) and from experimental measurements²⁰ (filled symbols), at 200 (diamonds), 240 (triangles), 270 (circles), and 300 K (squares).

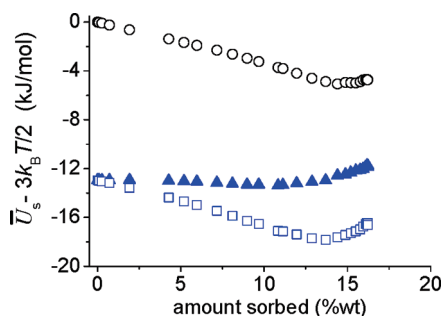


Figure 14. Same as Figure 4 for CH_4 at 240 K, using the M1D set of parameters.

It is observed that all model isotherms follow successfully the experimental trend, although overpredicting the data.

At this point, it must be stressed that the only physical entrances leading the guest molecules to the ZIF-8 cage are the hexagonal windows having an effective width of 0.34 nm,⁶ whereas the kinetic diameter of CH_4 is 0.38 nm. Grand canonical Monte Carlo sampling on the other hand, entails configurations resulting from nonphysical insertions and destructions of molecules over the entire sorbent framework, thereby leading to energetically acceptable configurations under the prescribed chemical potential. Incidentally, these algorithmic movements may also result in accepted configurations, including guests that reside in areas inside the sorbent matrix which, because of hindrance effects, would not be physically accessible by molecules.²⁸ Therefore, a reason for the higher simulation values with respect to the measurements, in addition to the possible inadequacy of the force field to match the measured data, is associated with the rigid organic group link, which reduces the effects of steric phenomena. In actual fact, recent neutron inelastic scattering and diffraction measurements in the ZIF-8 at very low temperatures revealed a quasi-free rotation of the methyl groups being higher than any other methylated compound.⁴⁴

The configurational internal energy of methane as a function of its occupancy in the imidazolate framework is presented in Figure 14. The sorbate–sorbent component of the total energy remains almost constant at low occupancies, presenting the expected tendency toward a smooth increase at higher loadings. Therefore, methane at 240 K perceives a lower energetic heterogeneity within the ZIF-8 sd compared to argon (cf. Figure 4).

Because of the aforementioned relative effective sizes between the six-ring windows and the methane molecule, its

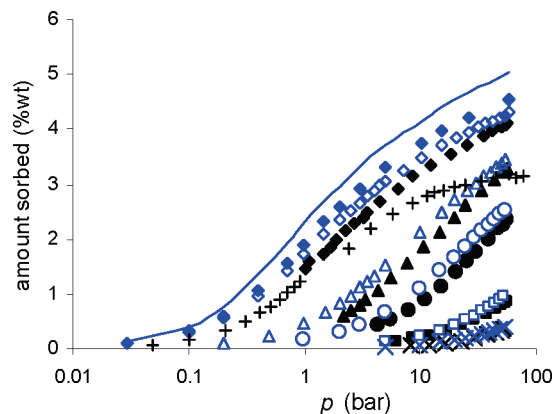


Figure 15. Sorption isotherms of H_2 in ZIF-8 from GCMC simulations using the Feynman-Hibbs quantum mechanical potential function for the calculation of interparticle interactions, along with the HD (open symbols) and HU (filled blue diamonds) sets of parameters, versus experimental measurements (black²⁰ and “+” symbols⁶), at 77 K (diamonds), 100 K (triangles), 125 K (circles), 200 K (squares), and 300 K (x symbols). The line represents simulations using the HD parameters set with no quantum correction at 77 K.

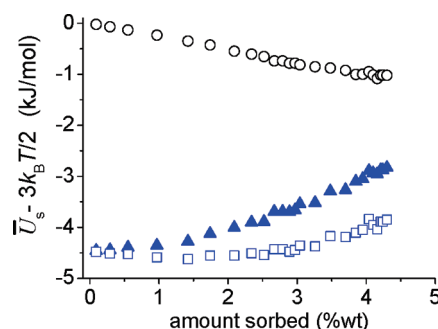


Figure 16. Same as Figure 14 for H_2 at 77 K, using the HD set of parameters.

molecular dynamics under an inflexible framework would lead to an artificial motion of the molecules being confined exclusively in the cage interior.

Figure 15 presents sorption predictions for hydrogen in the ZIF-8 over a wide range of temperatures toward a comparison between simulated and measured isotherms,^{6,20} along with a comparison of the two force fields for the description of the sorbent energetics (see Table 2). From the graphs of the above figure, is seen that through the DREIDING parametrization, the simulation results agree satisfactorily with the experimental data at all temperatures. Incorporation of quantum effects to all kinds of dispersion interactions proved to be the proper strategy, especially at very low temperatures, as can be seen from the discrepancy between the line representing results by means of the Lennard-Jones potential and the points in the same figure at the temperature of 77 K.

The partial molar internal energy of the sorbed phase at 77 K as a function of the hydrogen concentration in the ZIF-8 is illustrated in Figure 16. The total partial molar quantity shows the expected trend, increasing smoothly with increasing loading as a result of the declining pair energy part on the one hand, and the increasing sorbate–sorbent part on the other due to the progressively dropping binding energy.

In the graphs of Figure 17, results of density distribution functions for various hydrogen loadings in the ZIF-8 at 77 K are presented, aiming at mapping the preferred sites for hydrogen adsorption inside the metal–organic framework. The pair distribution function (Figure 17a) indicates a less structured

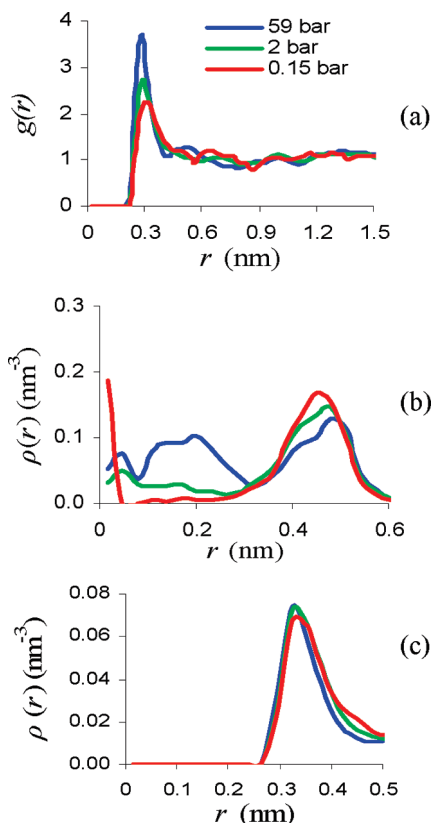


Figure 17. Pair distribution function of H₂ at 77 K (a) and density probability distributions calculated with respect to (b) the cage center and (c) the C=C bond.

adsorbed phase, as compared to the $g(r)$, observed in the case of argon at 87 K. Since both fluids were studied under nearly similar temperatures, the observed behavior of the pair distribution functions is attributed to their different strengths of interaction with the atomic framework. At higher pressures, the coordination number almost doubles, and our calculated nearest neighbor distance agrees with the value of 0.304 nm identified by means of neutron diffraction measurements of deuterium being fully adsorbed in the ZIF-8 at 3.5 K.⁴⁵

Figure 17b presents the calculated probability density distribution having as a reference point the cage center. It is seen that at low pressure, there is a broad probability of finding hydrogen molecules around the position of 0.45 nm from the cavity center, and a narrower distribution at the center which as loading increases tends to occupy a wider region at around 0.2 nm, in agreement with neutron diffraction measurements of deuterium in the ZIF-8.⁴⁵

Additional calculations having as reference the center of the C=C bonds of the imidazolate groups produced the graph of Figure 17c. The predicted distribution is peaked in the range between 0.29 and 0.36 nm, including two adsorption sites, also identified by neutrons at distances of 0.30 and 0.34 nm from the C=C bonds.⁴⁵ The latter distance corresponds to a site located close to the face center of the hexagonal window. The conclusion from our computations is that the organic link constitutes a primary adsorption site over the whole occupancy range employed in this study.

Eventually, by repeating the probability density calculations having the zinc atoms as a reference, we found none of the hydrogen molecules inside the unit cell to be close to the faces of the zinc tetrahedra, ZnN₄, which is in agreement with previous experimental findings.⁴⁵

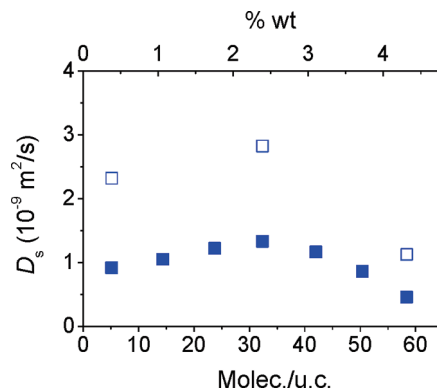


Figure 18. Self-diffusivity predictions of H₂ in the ZIF-8 at 77 K as a function of loading, using the HD set of parameters for the modeling of energetics. Employment of classical (open symbols) and quantum (filled symbols) potential functions are shown.

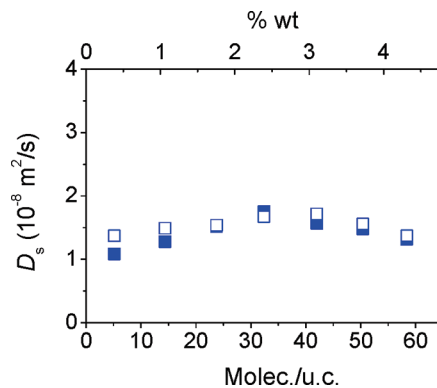


Figure 19. Same as Figure 18 at a temperature of 300 K.

The self-diffusivity of hydrogen inside the imidazolate framework at 77 K, calculated through eqs 4 and 5, are presented in Figure 18. A direct result from a modeling point of view is the remarkable deviation between the diffusivity values obtained when the dispersive interactions were computed through the Lennard-Jones potential and when the Feynman–Hibbs potential function was employed. From the analogous comparison between the sorption results shown in Figure 15 at 77 K, it is seen that quantum mechanics effects have a less pronounced impact on the thermodynamics. The diffusivity predictions at 300 K in Figure 19 show that the quantum mechanical description of hydrogen at ambient temperatures is unimportant.

The self-diffusivity of hydrogen in the ZIF-8 at 77 K increases monotonically with concentration up to about 2.4 wt % under 2 bar, and then decreases. This slight increase in diffusivity up to the shallow maximum corresponds to the progressive occupation of the site close to the cavity center (see Figure 17b). More specifically, the free energy minima (namely, the one located at the cavity center and the others close to C=C bonds, from 0.29 to 0.36 nm in Figure 17b) at low occupancies are separated by a high barrier as denoted by the almost zero density values at the site close to center (region surrounding the distance of 0.2 nm in Figure 17b). As pressure increases up to 2 bar, the free energy of the sites close to C=C also increases slightly. At the same time, the free energy of the mentioned site close to the center gradually decreases; hence, the aforementioned energy barrier does, as well, enhancing the molecular motion. As pressure further increases, the free energy barrier continues to decrease, resulting in an interplay with intermolecular collisions, which eventually predominate; therefore, mobility starts to decrease.

Recent molecular dynamics studies of hydrogen in the ZIF-68 and ZIF-70 at 298 K have resulted in values within the range of $(3-1.0) \times 10^{-8}$ and $(2-1.0) \times 10^{-7} \text{ m}^2 \text{ s}^{-1}$, respectively, as a function of loading.⁴⁶ Our predictions for ZIF-8 (Figure 19) have produced self-diffusivities varying with loading from 1.1×10^{-8} to $1.8 \times 10^{-8} \text{ m}^2 \text{ s}^{-1}$. The effective diameter of the ZIF-8 cavity is 1.16 nm, which is close to the ZIF-68 cavity size of 1.03 nm. The pore aperture width in the ZIF-8 is 0.34 nm, whereas the aperture size in the ZIF-68 is 0.75 nm.⁸ The narrower cavity-to-cavity paths in the ZIF-8 as well as the topology of the ZIF-68 and -70 (GME framework type) and their less mobile links with respect to the methyl group benzimidazolate and nitroimidazolate, respectively, can justify the slightly lower simulation values in the ZIF-8, and the almost 1 order of magnitude higher diffusivity of hydrogen in the ZIF-70 in comparison to the ZIF-8 and ZIF-68. ZIF-70 possesses a larger cavity (1.59 nm) and pore aperture width (1.31 nm). In addition, earlier simulation studies^{47,48} of hydrogen at 77 K on IRMOF-1, IRMOF-8, and IRMOF-18 and at 298 K on MOF-5 (or IRMOF-1)⁴⁹ support the fact that hydrogen mobility is affected by the relative aperture and cavity sizes as well as by the degree of hindrance imposed by the organic groups in the linking unit.

4. Conclusions

We have presented statistical-mechanics-based modeling of the sorption thermodynamics and dynamics of selected nonpolar molecules in the ZIF-8. Our aim was, first, to investigate the evolution of the sorption equilibrium in this material over a wide range of occupancies for Ar, CH₄, and H₂ up to saturation and, second, to elucidate the mechanism of molecular motion under the complicated force field exerted by the zinc atoms and the 2-methylimidazolate groups that form the void space of the organic zeolite analogue framework under study. For this purpose, we digitally reconstructed the ZIF-8 unit cell and then examined the applicability of generic force fields found in literature for the description of atomic-level interactions between sorbate molecules and framework atoms. We opted for the DREIDING force field after comparing the simulation predictions for the sorbates studied in this work with measured isotherms under the same conditions found elsewhere.

The partial molar configurational internal energy was calculated for Ar, CH₄, and H₂ as a function of their loading in the metal-organic framework at 87, 240, and 77 K, respectively, via grand canonical Monte Carlo simulations. Because the computed quantity is related to the covariance of the potential energy and number of particles at a certain loading and temperature, it can map the strength of sorbate-sorbate and sorbate-sorbent interactions over the full sorbate loading range. The results showed a higher perception of energetic inhomogeneity of argon in comparison with methane and hydrogen. One- and two-point probability density functions calculated by postprocessing the equilibrated configurations produced from Monte Carlo provided a further insight into the distribution of adsorption centers inside the ZIF-8 framework. Moreover, interpretation of these results on the basis of free energy distribution offered a plausible explanation of the mobility of the sorbed phase as a function of its chemical potential inside the metal-organic framework.

Although for hydrogen and argon the agreement between simulated and measured isotherms is satisfactory, the freezing of the degrees of freedom of the organic links in our model may cause the sitting transition step of the predicted isotherm of argon to appear earlier than the one observed experimentally.

It was also showed that such inflections during the sorption and kinetics procedure involve crossing of free-energy barriers located at positions near the six-ring window faces; therefore, the bonding flexibility at these areas may influence these barriers and, hence, the dynamics of guest molecules, even at low temperatures. The inflexibility of the model ZIF-8 unit cell can also be responsible for the overprediction of the sorption thermodynamics of the bulkier molecule of methane with respect to measured values found elsewhere.

The molecular mobility of Ar at 87 K and H₂ at 77 K inside the metal-organic sorbent was estimated by virtue of equilibrium molecular dynamics in the canonical ensemble. Although the self-diffusivity of argon at 87 K is too low to be of any practical importance, we observed its displacement over a broad range of occupancies in conjunction with the preceding thermodynamics findings to understand the kinetic behavior of the sorbed phase with respect to the calculated spatial partitioning of the sorbate probability density inside this new class of materials.

In view of the quantum nature of hydrogen at 77 K, we employed the path integral formulation for the quantum mechanical description of the intermolecular interactions, which leads to the quadratic Taylor expanded pairwise potential function, as follows from the work of Feynman and Hibbs. Their work states that paths located at a certain state point in the configuration space are enveloped inside a Gaussian width. For low temperatures and atomic masses, the distribution around this position becomes widespread; hence, a classical description is not adequate any more. The self-diffusivity of hydrogen in the ZIF-8 at 77 K as revealed by our molecular dynamics simulations showed a marked difference between the values obtained from the classical and quantum mechanical description of the energetics. The predicted self-diffusivity presents a shallow maximum as a function of occupancy due to the loading dependent free energy barrier, which separates the adsorption sites located close to the hexagonal windows and around the cavity center of the ZIF-8 unit cell.

At this point, we should stress that the rigidity of the model ZIF-8 framework should put one under serious consideration when simulation is carried out at high temperatures or guests whose size is commensurate with the effective size of critical paths for diffusion in the framework are involved. These issues are mainly associated with the rotation of the pendant alkyl or other groups of the imidazolate-type link as well as with possible torsional motions of the organic links themselves, which become much more pronounced with rising temperature. As a consequence, these phenomena may affect the dynamics of guest molecules inside the pore matrix, leading to unrealistic transport coefficients.

Acknowledgment. Support by the India-European Union collaborative project AMCOS (NMP3-SL-2009-233502), is gratefully acknowledged.

References and Notes

- (1) Yaghi, O. M.; Li, G.; Li, H. *Nature* **1995**, *378*, 703.
- (2) Li, H.; Eddaoudi, M.; Groy, T. L.; Yaghi, O. M. *J. Am. Chem. Soc.* **1998**, *120*, 8571.
- (3) Yaghi, O. M.; O'Keeffe, M.; Ockwig, N. W.; Chae, H. K.; Eddaoudi, M.; Kim, J. *Nature* **2003**, *423*, 705.
- (4) Chae, H. K.; Siberio-Pérez, D. Y.; Kim, J.; Go, Y.; Eddaoudi, M.; Matzger, A. J.; O'Keeffe, M.; Yaghi, O. M. *Nature* **2004**, *427*, 523.
- (5) Côté, A. P.; Benin, A. I.; Ockwig, N. W.; Matzger, A. J.; O'Keeffe, M.; Yaghi, O. M. *Science* **2005**, *310*, 1166.
- (6) Park, K. S.; Ni, Z.; Côté, A. P.; Choi, J. Y.; Huang, R.; Uribe-Romo, F. J.; Chae, H. K.; O'Keeffe, M.; Yaghi, O. M. *Proc. Natl. Acad. Sci. U.S.A.* **2006**, *103* (27), 10186.

- (7) Hayashi, H.; Côté, A. P.; Furukawa, H.; O'Keeffe, M.; Yaghi, O. M. *Nat. Mater.* **2007**, *6*, 501.
- (8) Banerjee, R.; Phan, A.; Wang, B.; Knobler, C.; Furukawa, H.; O'Keeffe, M.; Yaghi, O. M. *Science* **2008**, *319*, 939.
- (9) Düren, T.; Sarkisov, L.; Yaghi, O. M.; Snurr, R. Q. *Langmuir* **2004**, *20*, 2683.
- (10) Dubbeldam, D.; Frost, H.; Walton, K. S.; Snurr, R. Q. *Fluid Phase Equilib.* **2007**, *261*, 152–161.
- (11) Frost, H.; Snurr, R. Q. *J. Phys. Chem. C* **2007**, *111*, 18794.
- (12) Walton, K. S.; Millward, A. R.; Dubbeldam, D.; Frost, H.; Low, J. J.; Yaghi, O. M.; Snurr, R. Q. *J. Am. Chem. Soc.* **2008**, *130*, 406.
- (13) Garberoglio, G. *Langmuir* **2007**, *23*, 12154.
- (14) Han, S. S.; Furukawa, H.; Yaghi, O. M.; Goddard, W. A. *J. Am. Chem. Soc.* **2008**, *130*, 11580.
- (15) Klontzas, E.; Tylianakis, E.; Froudakis, G. E. *J. Phys. Chem. C* **2008**, *112*, 9095.
- (16) Furukawa, H.; Yaghi, O. M. *J. Am. Chem. Soc.* **2009**, *25*, 8876–8883.
- (17) Greathouse, J. A.; Kinnibrugh, T. L.; Allendorf, M. D. *Ind. Eng. Chem. Res.* **2009**, *48*, 3425.
- (18) Babarao, R.; Jiang, J. W.; Sandler, S. I. *Langmuir* **2009**, *25*, 5239.
- (19) Huang, X. C.; Lin, Y. Y.; Zhang, J. P.; Chen, X. M. *Angew. Chem., Int. Ed.* **2006**, *45*, 1557.
- (20) Zhou, W.; Wu, H.; Hartman, M. R.; Yildirim, T. *J. Phys. Chem. C* **2007**, *111*, 16131.
- (21) Wang, B.; Côté, A. P.; Furukawa, H.; O'Keeffe, M.; Yaghi, O. M. *Nature* **2008**, *453*, 207.
- (22) Morris, W.; Doonan, C. J.; Furukawa, H.; Banerjee, R.; Yaghi, O. M. *J. Am. Chem. Soc.* **2008**, *130*, 12626.
- (23) Liu, D.; Zheng, Ch.; Yang, Q.; Zhong, Ch. *J. Phys. Chem. C* **2009**, *113*, 5004.
- (24) Zhou, M.; Wang, Q.; Zhang, L.; Liu, Y.; Kang, Y. *J. Phys. Chem. B* **2009**, *113*, 11049.
- (25) Yaghi's group resynthesized (see ref 6) the ZIF-8 using a different, more efficient way than the originally reported in ref 19.
- (26) Mayo, S. L.; Olafson, B. D.; Goddard, W. A., III *J. Phys. Chem.* **1990**, *94*, 8897.
- (27) Rappé, A. K.; Casewit, C. J.; Colwell, K. S.; Goddard, W. A., III; Skiff, W. M. *J. Am. Chem. Soc.* **1992**, *114*, 10024.
- (28) Pantatosaki, E.; Papadopoulos, G. K. *J. Chem. Phys.* **2007**, *127*, 164723.
- (29) Papadopoulos, G. K.; Theodorou, D. N. *Mol. Simul.* **2009**, *35*, 79.
- (30) Sant, M.; Leyssale, J.-M.; Papadopoulos, G. K.; Theodorou, D. N. *J. Phys. Chem. B* **2009**, *113*, 13761.
- (31) Feynman, R. P.; Hibbs, A. R. *Quantum Mechanics and Path Integrals*; McGraw-Hill: New York, 1965.
- (32) Seehamart, K.; Nanok, T.; Krishna, R.; van Baten, J.-M.; Remsungnen, T.; Fritzsche, S. *Microporous Mesoporous Mater.* **2009**, *125*, 97.
- (33) Amirjalayer, S.; Tafipolsky, M.; Schmid, R. *Angew. Chem., Int. Ed.* **2007**, *46*, 463.
- (34) Greathouse, J. A.; Allendorf, M. D. *J. Phys. Chem. C* **2008**, *112*, 5795.
- (35) Dubbeldam, D.; Walton, K. S.; Ellis, D. E.; Snurr, R. Q. *Angew. Chem., Int. Ed.* **2007**, *46*, 4496.
- (36) Pantatosaki, E.; Papadopoulos, G. K.; Jovic, H.; Theodorou, D. N. *J. Phys. Chem. B* **2008**, *112*, 11708.
- (37) García-Peréz, E.; Parra, J. B.; Ania, C. O.; Dubbeldam, D.; Vlugt, T. J. H.; Castillo, J. M.; Merklings, P. J.; Calero, S. *J. Phys. Chem. C* **2008**, *112*, 9976.
- (38) Hirschfelder, J. O.; Curtiss, C. F.; Bird, R. B. *Molecular Theory of Gases and Liquids*; Wiley: New York, 1954.
- (39) Goodbody, S. J.; Watanabe, K.; MacGowan, D.; Walton, J. P. R. B.; Quirke, N. *J. Chem. Soc. Faraday Trans.* **1991**, *87*, 1951.
- (40) Dubbeldam, D.; Calero, S.; Vlugt, T. J. H.; Krishna, R.; Maesen, T. L. M.; Smit, B. *J. Phys. Chem. B* **2004**, *108*, 12301.
- (41) Allen, M. P.; Tildesley, D. J. *Computer Simulation of Liquids*; Clarendon Press: Oxford, 1987.
- (42) Vlugt, T. J. H.; Schenk, M. *J. Phys. Chem. B* **2002**, *106*, 12757.
- (43) Guse, M. P.; Kunz, A. B. *Phys. Status Solidi* **1975**, *71*, 631.
- (44) Zhou, W.; Wu, H.; Udovic, T. J.; Rush, J. J.; Yildirim, T. *J. Phys. Chem. A* **2008**, *112*, 12602.
- (45) Wu, H.; Zhou, W.; Yildirim, T. *J. Am. Chem. Soc.* **2007**, *129*, 5314.
- (46) Rankin, R. B.; Liu, J.; Kulkarni, A. D.; Johnson, J. K. *J. Phys. Chem. C* **2009**, *113*, 16906.
- (47) Yang, Q.; Zhong, Ch. *J. Phys. Chem. B* **2005**, *109*, 11862.
- (48) Liu, B.; Yang, Q.; Xue, Ch.; Zhong, Ch.; Smit, B. *Phys. Chem. Chem. Phys.* **2008**, *10*, 3244.
- (49) Skoulidas, A. I.; Sholl, D. S. *J. Phys. Chem. B* **2005**, *109*, 15760.